JAERI-M
90-211

ENERGY CONVERSION EFFICIENCY IN HIGH CURRENT RAMAN-REGIME FREE-ELECTRON LASER

II. MULTI-MODE ANALYSIS

November 1990

Yasuaki KISHIMOTO, Hisako ODA* and Makoto SHIHO

日本原子力研究所
Japan Atomic Energy Research Institute

JAERI-Mレポートは，日本原子力研究所が不定期に公刊している研究報告書です。
入手の問合わせは，日本原子力研究所技術情報部情報資料課（〒319－11茨城県那珂郡東海村）あて，お申しこしください。なお，このほかに財団法人原子力弘済会資料センター（〒319-11茨城県那珂郡東海村日本原子力研究所内）で複写による実費頒布をおこなっております。

JAERI-M reports are issued irregularly.
Inquiries about availability of the reports should be addressed to Information Division, Department of Technical Information, Japan Atomic Energy Research Institute, Tokai-mura, Naka-gun, Ibaraki-ken 319-11, Japan.

編集兼発行　日本原子力研究所
印　　刷　日立高速印刷株式会社

JAERI-M 90-211

Energy Conversion Efficiency in High Current Raman-Regime Free-Electron Laser II. Multi-mode analysis

Yasuaki KISHIMOTO, Hisako ODA* and Makoto SHIHO

Department of Thermonuclear Fusion Research
Naka Fusion Research Establishment
Japan Atomic Energy Research Institute
Naka-machi, Naka-gun, Ibaraki-ken

(Received November 2, 1990)

Parasitic wave excitation in a Raman-regime free-electron laser(FEL) was investigated in Phys. Rev. Lett. 65, 851(1990)(ref. 9) by using a one dimensional multi-frequency amplification code. It was found that multi-mode coupling among sideband waves and and the primary wave plays an important role in the parasitic wave excitation in addition to the sideband instability. We here describe the details of the numerical calculation and study the underlying physical mechanisms leading to the observed results. The origin of the new wave excitation by the multi-mode coupling is found to be a forced oscillation due to the transverse nonlinear current produced by the mode coupling. Especially. "an additive law" for the growth rate of parasitic waves observed in the above reference(ref.9) is analytically deduced.

Keywords: Free Electron Laser, Raman FEL, Side-band Instability
Parasitic Wave Excitation, Multi-mode Coupling

* Kanazawa Computer Service Corp.

高電流ラマン領域自由電子レーザーにおけるエネルギー変換効率
Ⅱ．多モード解析

日本原子力研究所那珂研究所核融合研究部
岸本　泰明・小田　久子*・志甫　諒

（1990年11月2日受理）

ラマン領域自由電子レーザー（ＦＥＬ）における寄生波励起が１次元多周波数増幅コードを用いて，Phys．Rev．Lett．65，851（1990）（参考文献９）において調べられた。そこでは，サイドバンド不安定性に加え，サイドバンド波と主要波間のモード結合が寄生波励起に重要な役割を果すことが明らかになった。ここでは，その数値計算の詳細を述べると共に，得られた結果に導く基礎となる物理機構について調べる。多モード結合による新しい波の励起の起源は，モード結合によって生じた縦方向の非線形電流による強制振動であることがわかった。とりわけ上記の文献（参考文献９）で観測された寄生波の成長率に対する＂加算法則＂が解析的に導き出された。

那珂研究所：〒311－01　茨城県那珂郡那珂町大字向山801－1
＊（株）カナザワコンピューターサービス

Contents

目　　次

1. Introduction

Analysis of a parasitic wave excitation in the Free Electron Laser is important to determine the quality of an output radiation signal. Most of the previous analytical[1-4] and computational[5-7] works about the parasitic wave was concerned with a sideband instability in a Compton regime where a frequency shift from a primary field is relatively small, i.e. $|\Delta\omega_{sb}|\ (\equiv|\omega_{sb}-\omega_0|)\ll\omega_0$ (ω_0 and ω_{sb} denote the angular frequency of the primary field and the sideband one), but rarely in a Raman regime[8]. In the high current Raman regime where the radiation power density is quite high, a significant frequency modulation is possible to take place because the frequency shift $|\Delta\omega_{sb}|$ due to the sideband instability is roughly proportional to the electron bounce frequency Ω_B in a ponderomotive potential of the primary signal. A.T.Lin first investigated the parasitic wave excitation in the Raman regime by using the 1-2/2 electromagnetic particle code and found that wave shifted to the low-frequency side grow with a larger growth rate than that of the primary wave as a result of the sideband instability[8]. Such a significant modulation of the primary signal might also induce the different type of the parasitic wave.

In ref.9, we present a different type of the excitation mechanism of the parasitic wave in the Raman regime in addition to the so-called sideband instability discussed by the literatures[1-8]. The mechanism is due to the multi-mode coupling among different frequency waves, which generally exists in the system by the sideband instability and the linear FEL amplification. Such multi-mode coupling are observed in both linear and nonlinear trapping stages and modulate the output signal to a comparable level with that solely due to the sideband instability. In the present paper, we describe the details of the numerical calculation of the ref.9 and study the underlying physical mechanisms leading to the observed results. To qualitatively

understand the phenomena of the multi-mode coupling, we introduce a model where two radiation fields with a large amount of energy are injected into the wiggler as inputs. The origin of the new wave excitation by the multi-mode coupling is found to be a forced oscillation due to the transverse current produced by the mode coupling. Especially, "an additive law" for the growth rate of parasitic(and/or sideband) waves which is observed in the ref.9 is analytically obtained.

In Sec.2, we present the basic equations and the numerical method of the 1-dimensional multi-frequency FEL code. Two-wave calculations with a primary field and single sideband are presented in Sec.3-1. The mode coupling process among different frequency waves is analytically investigated in Sec.3-2. In Sec.3-3, we develop the calculation to cases where multi-sideband waves exist. Sec.5 summarizes our conclusion.

2. Basic Equations and Numerical Method

The physical model we employed here is a 1-dimensional relativistic electron beam interacting with a spatially periodic helical wiggler field :

$$A_w(z) = -A_w(z)\,(\mathbf{e}_x \cos \int k_w dz + \mathbf{e}_y \sin \int k_w dz) \quad ,$$

and radiation and electrostatic fields which are Fourier-decomposed as

$$A(z,t) = \sum_m A_m(z)\,(\mathbf{e}_x \cos \hat{\psi}_m - \mathbf{e}_y \sin \hat{\psi}_m) \quad , \tag{1}$$

$$\Phi(z,t) = \sum_m \Phi_m(z) \cos \hat{\psi}_{em}, \qquad \text{for } m=0, \pm 1, \pm 2, \ \ldots\ldots \tag{2}$$

where

$$\hat{\psi}_m(z) = \int_0^z k_{+m}(z')dz' - \omega_m t + \theta_m \quad \text{and} \quad \hat{\psi}_{em}(z) = \int_0^z k_m(z')dz' - \omega_m t + \alpha_m .$$

understand the phenomena of the multi-mode coupling, we introduce a model where two radiation fields with a large amount of energy are injected into the wiggler as inputs. The origin of the new wave excitation by the multi-mode coupling is found to be a forced oscillation due to the transverse current produced by the mode coupling. Especially, "an additive law" for the growth rate of parasitic(and/or sideband) waves which is observed in the ref.9 is analytically obtained.

In Sec.2, we present the basic equations and the numerical method of the 1-dimensional multi-frequency FEL code. Two-wave calculations with a primary field and single sideband are presented in Sec.3-1. The mode coupling process among different frequency waves is analytically investigated in Sec.3-2. In Sec.3-3, we develop the calculation to cases where multi-sideband waves exist. Sec.5 summarizes our conclusion.

2. Basic Equations and Numerical Method

The physical model we employed here is a 1-dimensional relativistic electron beam interacting with a spatially periodic helical wiggler field :

$$A_w(z) = -A_w(z)\,(\mathbf{e}_x \cos \int k_w dz + \mathbf{e}_y \sin \int k_w dz) \quad ,$$

and radiation and electrostatic fields which are Fourier-decomposed as

$$A(z,t) = \sum_m A_m(z)\,(\mathbf{e}_x \cos \hat{\psi}_m - \mathbf{e}_y \sin \hat{\psi}_m) \quad , \tag{1}$$

$$\Phi(z,t) = \sum_m \Phi_m(z) \cos \hat{\psi}_{em}, \qquad \text{for } m=0, \pm 1, \pm 2, \ \ldots\ldots \tag{2}$$

where

$$\hat{\psi}_m(z) = \int_0^z k_{+m}(z')\,dz' - \omega_m t + \theta_m \quad \text{and} \quad \hat{\psi}_{em}(z) = \int_0^z k_m(z')\,dz' - \omega_m t + \alpha_m .$$

Here, $\omega_m/2\pi$ is the frequency of mode m ($\omega_{m=0}=\omega_0$ denotes the primary signal), and k_{+m} and k_m are corresponding wave numbers. θ_m and α_m is the initial electron phases. In Eq.(1), electromagnetic fields are assumed to be a right-handed circularly polarized wave.

Here, we assume that $\Delta\omega=\omega_0/N$ (N : integer) is a minimum frequency difference between two adjacent modes. Therefore, the nonlinear driving current J_{NL} in Maxwell's equations has to be determined from a particle dynamics extended over a long interaction time scale $\Delta T=2\pi/\Delta\omega$. Substituting $A(z,t)$ and $\Phi(z,t)$ together with the microscopic current density into the Maxwell's equations, we obtain non-wiggler averaged field equations for slowly varying parts for mode m : $a_m=eA_m/mc^2$ and $\phi_m=e\Phi_m/mc^2$, as follows,

$$\frac{\partial^2 a_m}{\partial z^2}+\left(\frac{\omega_m^2}{c^2}-k_{+m}^2\right)a_m=\frac{\omega_b^2}{c^2}\left\langle\frac{\beta_{z0}}{v_z}(v_1\cos\psi_m-v_2\sin\psi_m)\right\rangle_m, \tag{3}$$

$$2k_{+m}^{1/2}\frac{\partial}{\partial z}\left(k_{+m}^{1/2}a_m\right)=-\frac{\omega_b^2}{c^2}\left\langle\frac{\beta_{z0}}{v_z}(v_1\sin\psi_m+v_2\cos\psi_m)\right\rangle_m, \tag{4}$$

$$\frac{\partial\phi_m}{\partial z}=-\frac{2\omega_b^2}{c\omega_m}\langle\beta_{z0}\sin\hat{\psi}_{em}\rangle_m, \tag{5}$$

$$k_m\phi_m=-\frac{2\omega_b^2}{c\omega_m}\langle\beta_{z0}\cos\hat{\psi}_{em}\rangle_m, \qquad \text{for } m=0,\pm1,\pm2,\ \ldots. \tag{6}$$

where $\psi_m=\hat{\psi}_m+\int k_w dz$, $\omega_b^2=4\pi e^2 n_b/m$ (n_b: the beam density), and (v_1, v_2) denote perpendicular components of an electron velocity described by a helical coordinate. β_{z0} is defined by $v_z(t=t_0)/c$, where t_0 represents the time when the electron enters the interaction region at $z=0$. In deriving eqs.(3)-(6), the Coulomb gauge is employed. An initial electron phase $\psi_{0m}=-\omega_m t_0$ in ψ_m and ψ_{em} extends over $\{-\omega_m\pi/\Delta\omega,\ +\omega_m\pi/\Delta\omega\}$. $\langle(\ldots)\rangle_m$ in Eqs.(3) to (6) represents

an average with respect to ψ_{0m} and an initial electron momentum distribution $f_b(p_0)$ which is defined by

$$\langle\ (\ldots)\ \rangle=\frac{1}{2\pi n_b}\int_{+\omega_m\pi/\Delta\omega}^{-\omega_m\pi/\Delta\pi} d\psi_{0m}\int f_b(p_0)(\ldots)dp_0.$$

Equations (3) to (6) couple to $3N_T$ (N_T: number of test particle) electron motion equations. In the initial state, test particles are uniformally distributed in the phase space to provide the input radiation power as an extenal parameter.

In the numerical calculation, a millimeter radiation field of f=60GHz is injected as a primary radiation. A beam energy E_b=1MeV (γ_b≃2.96), beam current density I_b=1.5kA/cm^2, constant wiggler pitch λ_w(=2π/k_w)=4cm, and wiggler field B_w≃1.94KG are employed. The wiggler field is adiabatically increased in an entry region $0\le z\le 10\lambda_w$. The initial level of the electrostatic potential

$$\phi_m(z=0)=\frac{-2\omega_b^2}{c\omega_m(k_{+m}+k_w)}\langle\beta_{z0}\cos\psi_{em}\rangle$$

is determined from a numerical error which corresponds to an initial setting of test particles in the phase space[10]. In the paper, we only consider the non-tapered wiggler case. No axial beam energy spread and no axial guide field are also assumed. Note that parameters employed here belong to the strong Raman scattering regime.

3. Numerical Results and Discussions

In Sec.3-1, we present numerical results in single sideband case.

an average with respect to ψ_{0m} and an initial electron momentum distribution $f_b(p_0)$ which is defined by

$$\langle\ (\ldots)\ \rangle=\frac{1}{2\pi n_b}\int_{+\omega_m\pi/\Delta\omega}^{-\omega_m\pi/\Delta\pi} d\psi_{0m}\int f_b(p_0)(\ldots)dp_0.$$

Equations (3) to (6) couple to $3N_T$ (N_T: number of test particle) electron motion equations. In the initial state, test particles are uniformally distributed in the phase space to provide the input radiation power as an extenal parameter.

In the numerical calculation, a millimeter radiation field of f=60GHz is injected as a primary radiation. A beam energy E_b=1MeV ($\gamma_b\simeq2.96$), beam current density I_b=1.5kA/cm^2, constant wiggler pitch $\lambda_w(=2\pi/k_w)$=4cm, and wiggler field $B_w\simeq1.94$KG are employed. The wiggler field is adiabatically increased in an entry region $0\leq z\leq10\lambda_w$. The initial level of the electrostatic potential

$$\phi_m(z=0)=\frac{-2\omega_b^2}{c\omega_m(k_{+m}+k_w)}\langle\beta_{z0}\cos\psi_{em}\rangle$$

is determined from a numerical error which corresponds to an initial setting of test particles in the phase space[10]. In the paper, we only consider the non-tapered wiggler case. No axial beam energy spread and no axial guide field are also assumed. Note that parameters employed here belong to the strong Raman scattering regime.

3. Numerical Results and Discussions

In Sec.3-1, we present numerical results in single sideband case.

Before the presentation of multi-sideband results in Sec.3-3, a qualitative discussion of the mode coupling among different frequency waves is done in 3-2. The growth rate and the saturation efficiency by the single mode analysis were studied in Ref.10.

3.1 Single Sideband Case

Figure 1(a) shows typical spatial evolutions of radiation and space charge fields for the f=60GHz primary wave and the f=40GHz sideband. An initial input power at z=0 is chosen to $P_{in,60}=10^{3}$W/cm^{2} for the primary field and $P_{in,40}=10^{-3}$W/cm^{2} for the sideband one. After the saturation of the primary wave ($\hat{z}_{sat}(\equiv z_{sat}/\lambda_w)\simeq 16$), the f=40GHz wave which has no linear FEL amplification grows exponentially by the sideband instability with the growth rate of Γ_{40} ($\equiv d\ln a_{40}/dz)\simeq 0.16$cm^{-1} both for the radiation and the space charge fields. The sideband wave overtakes the primary one at around $\hat{z}\equiv z/\lambda_w\simeq 36$ and then saturates. Spatial evolution of the trapped particle fraction due to both f=60 and 40GHz ponderomotive potentials is illustrated in Fig.1(b). An average trapping fraction due to the primary potential ($\langle\delta_{60}\rangle$) is about 75% when the amplitude of the sideband wave is enough low, i.e. $a_{40}/a_{60}\lesssim 10^{-2}$. As the sideband wave grows i.e. $a_{40}/a_{60}\lesssim 1$, electrons trapped by the primary potential are detrapped down to $\langle\delta\rangle_{60}\simeq 52\%$, whereas the sideband one increases up to $\langle\delta\rangle_{40}\simeq 52\%$. To see the above process, particle positions and the separatrix(solid line) in a phase space for the primary wave, i.e. ($\psi_{m=0}$, $d\psi_{m=0}/dz$), are shown in Fig.1(c) from $\hat{z}(\equiv z/\lambda_w)$=30 to 60. Here, the separatrix is is given by

$$S(\psi_{m=0},\frac{d\psi_{m=0}}{dz})\equiv\left(\frac{d\psi_{m=0}}{dz}\right)^{2}-\frac{8a_w a_s k_w^{2}}{\gamma_i^{2}}(1+\cos\psi_{m=0})=0, \tag{7}$$

where $\gamma_\perp=1+a_w^2$. Thus, the saturation of the sideband originates from the separatrix overlapping with the primary potential. The sideband amplitude a_m to cause the separatrix overlapping with a m=0 primary wave is estimated from eq.(7) as

$$a_m \simeq \frac{\gamma_\perp^2}{16a_w}\left\{\left(1+\frac{k_{+m}}{k_w}\right)-\frac{\omega_m}{\omega_{m=0}}\left(1+\frac{k_{+m=0}}{k_w}\right)\left(1+\frac{\beta_{m=0}v_{pm=0}}{\omega_{m=0}}\right)\right\}^2 \tag{8}$$

$$\text{for} \quad v_{pm}<\frac{v_{pm=0}\omega_{m=0}}{\omega_{m=0}+v_{pm=0}\beta_{m=0}} \quad \text{or} \quad v_{pm}>\frac{v_{pm=0}\omega_{m=0}}{\omega_{m=0}-v_{pm=0}\beta_{m=0}}$$

where $v_{pm}=\omega_m/(k_{+m}+k_w)$ and $\beta_m=4(a_wa_m)^{1/2}k_w/\gamma_\perp$. In the present case, the phase velocity of the sideband potential v_{p40} satisfies the relation $v_{p60}\omega_{60}/(\omega_{60}+v_{p60}\beta_{60})<v_{40}<v_{p60}$ for $\hat{z}\gtrsim 16$, the two separatrixes overlap in an initial stage of the sideband instability. Since the phase velocity of the sideband potential v_{p40} is smaller than v_{p60}, electrons are detrapped releasing the kinetic energy to the lower frequency sideband without significantly reducing the power level of the primary field.

The result for the f=20GHz sideband case is shown in Fig.2(b). The growth rate of the sideband measured from the saturation point of the primary field is smaller ($\Gamma_{20,a}\simeq 0.1\text{cm}^{-1}$) than that of the f=40GHz case(Fig.1(a)). The result indicates that the f=20GHz wave is rather off-resonant for the sideband instability compared with the f=40GHz wave. Figure 1(b) also shows that the growth rate of the sideband instability changes at around $\hat{z}\simeq 35$ and gives a smaller value ($\Gamma_{20,b}\simeq 0.025\text{cm}^{-1}$) for $\hat{z}\gtrsim 35$. Such a change of the growth rate is considered as an effect of the longitudinal electrostatic interaction which comes from the high beam current density. That is, in $\hat{z}_{sat}\lesssim\hat{z}\lesssim 35$, the electrostatic force $f_{es}=e\partial\Phi/\partial z$ prevents the harmonic electron bounce motion in the ponderomotive potential[11]. An irregular electron

motion modulates the bounce frequency Ω_B and the related sideband instability. On the other hand, the electrostatic interaction leads the phase scrambling of bunched electrons which reduces the electrostatic force f_{es}. The reduction of f_{es} in $\hat{z} \gtrsim 35$ restores the harmonic electron motion and the corresponding growth rate of the sideband instability[12]. Therefore, the region of $\hat{z}_{sat} \lesssim \hat{z} \lesssim 35$ is recognized as a relaxation layer of the electrostatic interaction.

Frequency spectrum of the sideband growth rate Γ_{sb} is shown in Fig.3. Here, Γ_{sb} is measured after the saturation of the f=60GHz primary wave. An asymmetric Γ_{sb} spectrum, where lower sidebands exhibit a strong instability, is obtained in accordance with theoretical indications[2-4]. The typical frequency shift from the primary wave $\Delta\omega_{s,max}/2\pi$ is about 20GHz. Evaluating the bounce frequency by use of a relation[1,2] $\Omega_B \simeq 2ck_w\sqrt{a_w\langle a_r\rangle/(1+a_w^2)}$, we estimate the frequency shift as $\Delta\omega_{s,max}/2\pi \simeq k_{+m=0}\Omega_B/2\pi k_w \simeq 14$GHz by applying a_w=0.725 and $\langle a_r\rangle \simeq 0.03$, which is roughly the same order as the numerical calculation. In Fig.3, $\Delta\omega_F/2\pi \simeq 20$GHz represents the typical frequency width of the linear growth rate of the primary wave.

3.2 Analysis of Mode Coupling

Up to now, we considered the single sideband cases. Here, we develop the analysis to cases where the multi-sideband waves simultaneously exist. In such a case, various mode couplings among different frequency waves will play an important role for determining the output radiation spectrum.

In this section, we first assume two radiation fields with a large amount of energy as

$$A(z,t) = \sum_{q=1,2} A_q \mathbf{e}_+ \exp\left[i\left(k_q z - \omega_q t + \theta_q\right)\right] + \text{c.c.} \quad , \tag{9}$$

assuming the right handed circularly polarized one, where $e_+=(e_x+ie_y)/2$. Then, the beat field with ($\Delta\omega=\omega_1-\omega_2$, $\Delta k_+=k_{+1}-k_{+2}$) is excited through the nonlinear term of $[p\times(\nabla\times A)]_z$ in the electron motion equation and the longitudinal momentum and density modulations:

$$\delta p_s = \frac{e^2\Delta k_+ A_1 A_2^*}{2\gamma_b mc^2(\Delta\omega-\Delta k_+ v_b)} \exp[i(\Delta k_+ z-\Delta\omega t)] + c.c., \tag{10}$$

$$\delta n_s = \frac{e^2 n_b \Delta k_+^2 A_1 A_2^*}{2\gamma_b^4 m^2 c^2(\Delta\omega-\Delta k_+ v_b)^2} \exp[i(\Delta k_+ z-\Delta\omega t)] + c.c., \tag{11}$$

are induced. Note that such a nonlinear coupling comes not only from the above nonlinear term but also from $(v\cdot\nabla)p$ in the motion equation as well as $\nabla\cdot(nv)$ in the continuity equation and provides the same order contributions as $[p\times(\nabla\times A)]_z$ term. Note in that case that the radiation field with $(\omega_1+\omega_2, k_{+1}+k_{+2})$ is also excited. Since the beam modulation given by eqs.(10) and (11) propagates with the phase velocity $v_p\simeq(\omega_1-\omega_2)/(k_{+1}-k_{+2})\sim c$, a resonant interaction between the beam modulation $(\delta n_s, \delta p_s)$ and the ponderomotive potential ($v_p=\Delta\omega/(\Delta k_+ + k_w)$) formed by the radiation field with $(\Delta\omega, \Delta k_+)$ and the wiggler field does not take place.

The density modulation, however, will act on the radiation field with $\omega\sim\Delta\omega$ as a forced term through the coupling with the wiggler field. That radiation satisfies the following wave equation,

$$\left\{\frac{\partial^2}{\partial z^2} + \frac{1}{c^2}\left(\Delta\omega^2-\frac{\omega_b^2}{\gamma_b}\right)\right\}\tilde{A}_s(z) = \frac{4\pi e n_b}{\gamma_b mc} p_{x0}\delta\hat{n}\exp[i\Delta k_+ z], \tag{12}$$

and $$\delta\hat{n}_s=\delta n_s/n_b=\frac{c^2\Delta k_+^2 a_1 a_2^*}{\gamma_b^4(\Delta\omega-\Delta k_+ v_b)^2}\sim 4a_1 a_2^*,$$

where $p_{0x}=-(m\Omega_w/k_w)\cos k_w z$, $\Omega_w \equiv eB_w/mc$, and $A_s(z)=\tilde{A}_s \mathbf{e}_+ \exp(i\Delta\omega t)$ + c.c. In eq.(12), we neglect the perpendicular perturbation of the electron $p_\perp \propto \exp[i(\Delta k_+ z - \Delta\omega t)]$, which will be also produced through the nonlinear term of $[p\times(\nabla\times A)]_\perp$.

The general solution of eq.(12) is given as follows,

$$\tilde{a}_s=\tilde{a}_{s0}\exp(ik_{+s}z) - \frac{1}{2}\xi^2\hat{\Omega}_w\delta\hat{n}k_w^2\left\{\frac{\exp[i(\Delta k_+-k_w)z]}{[k_{+s}^2-(\Delta k_+-k_w)^2]}+\frac{\exp[i(\Delta k_++k_w)z]}{[k_{+s}^2-(\Delta k_++k_w)^2]}\right\} \quad (13)$$

where $\Delta\omega^2=c^2k_{+s}^2+\omega_b^2$, $\xi \equiv \omega_b/\gamma_b^{1/2}ck_w$, $\hat{\Omega}_w \equiv \Omega_w/ck_w$, $\tilde{a}_s=e\tilde{A}_s/mc^2$, and $\tilde{a}_{s0}$ is the initial amplitude of $\tilde{a}_s$. It is found in the second term of R.H.S in eq.(13) that the radiation field with the wave number shifted up and down by k_w from Δk_+ is excited. When the initial radiation(eq.(9)) has an enough power in it, i.e. $a_1 a_2^* > \tilde{a}_{s0}[k_{+s}^2-(\Delta k_+-k_w)^2]/2\xi^2\hat{\Omega}_w$, the amplitude of the forced term exceeds the one with the natural frequency. However, it should be noted that the radiation induced by the forced oscillation does not satisfy the dispersion relation in a vacuum. Such a radiation will come out only when a transition of the wave number, i.e. $\Delta k_+ \pm k_w \rightarrow \Delta k_+ \sim k_{+s}$ takes place inside the beam.

When the initial amplitude has the exponential growth rate such as $a_1 \sim \exp(\Gamma_1 z)$ and $a_2 \sim \exp(\Gamma_2 z)$, the solution of eq.(13) is rewritten as

$$\tilde{a}_s=\tilde{a}_{s0}\exp(ik_{+s}z) - \frac{1}{2}\xi^2\hat{\Omega}_w\delta\hat{n}k_w^2\left\{\frac{\exp[i(\Delta k_+-k_w)z+(\Gamma_1+\Gamma_2)z]}{[k_{+s}^2+(\Gamma_1+\Gamma_2)^2-(\Delta k_+-k_w)^2+2i(\Gamma_1+\Gamma_2)(\Delta k_+-k_w)]}\right.$$
$$\left. + (k_w \rightarrow -k_w)\right\}, \quad (14)$$

which also grow exponentially following the additive law, i.e. $\Gamma_1+\Gamma_2$.

We now expect the second coupling between the lower frequency modulation(eqs.(10) and (11)) and the modulation induced by the initial radiations(eq.(9)), through the nonlinear term of $(v_z\partial/\partial z)p_z$ and $\partial(nv_z)/\partial z$ in the motion and continuity equations. That is, $(\delta n_s,\delta p_s)$ couples to $(\delta n_1,\delta p_1)$ and $(\delta n_2,\delta p_2)$, and symmetrically creates the upper and lower sideband modulations $(\delta n_3,\delta p_3)$ and $(\delta n_4,\delta p_4)$ with $(\omega_1+\Delta\omega,k_{+1}+\Delta k_+ +k_w)$ and $(\omega_2-\Delta\omega,k_{+2}-\Delta k_+ +k_w)$. In the linear stage of the FEL amplification, $(\delta p_{1,2},\delta n_{1,2})$ are given by

$$\delta p_{1,2} = \frac{e\Omega_w(k_{+1,2}+k_w)A_{1,2}}{2\gamma_b ck_w[\omega_{1,2}-(k_{+1,2}+k_w)v_b]}\exp[i(k_{+1,2}+k_w)z-\omega_{1,2}t)] + c.c.$$

$$\delta n_{1,2} = -\frac{en_b\Omega_w(k_{+1,2}+k_w)^2A_{1,2}}{2m\gamma_b^4ck_w[\omega_{1,2}-(k_{+1,2}+k_w)v_b]^2}\exp[i(k_{+1,2}+k_w)z-\omega_{1,2}t)] + c.c.$$

The density modulation $(\delta n_3,\delta n_4)$ also act on the radiations with $(\omega_1+\Delta\omega,\omega_2-\Delta\omega)$ as a forced term through the coupling with the wiggler field same as eq.(12). In the second coupling, the wave number of the radiation induced by the forced oscillation is given by $(k_{+1}+\Delta k_+$ or $k_{+1}+\Delta k_+ +2k_w$)and $(k_{+2}-\Delta k_+$ or $k_{+1}-\Delta k_+ +2k_w$). If the waves $(\omega_1+\Delta\omega,k_{+1}+\Delta k_+)$ and $(\omega_2-\Delta\omega,k_{+2}-\Delta k_+)$ are excited, these radiations satisfy the dispersion relation in the vacuum.

The process will be successively repeated and creates the symmetrical sidebands around the initial two radiation fields(eq.(9)) together with the first excited lower frequency field. When the initial two radiations have the linear growth rate, the sidebands exponentially grow and the growth rate of that wave becomes larger with an increasing number of the mode coupling following the additive law.

3.3 Multi Sidebands Case

Figure 4(a) shows the result in which the f=40GHz and f=20GHz sidebands are both included. It is found that the f=20GHz wave grows following the growth rate of the f=40GHz sideband and shows a different feature as Fig.2. This result is interpreted by the previous mode coupling analysis : beat field between the primary radiation and the f=40GHz sideband induces the beam modulation $(\delta n_s, \delta p_s)$: the beam modulation couples to the wiggler field and forces to excite the f=20GHz wave. The growth rate is also interpreted from the argument of eq.(14) as $\Gamma_{20} \simeq \Gamma_{60} + \Gamma_{40} \simeq \Gamma_{40}$, because of $\Gamma_{40} \simeq 0$ in the saturation stage.

Figure 4(c) illustrates the wave number of each radiation field. It is found that the wave number of f=20GHz field(natural value is $k_{+20} \simeq 2.64 k_w$) is locked to the down shifted value nearly by k_w, i.e. $k_{+20} \simeq 1.6 k_w$ at around $\hat{z}$=24, where the f=20GHz field starts to grow. That is, the numerical result indicates that the term proportional to $\exp[i(\Delta k_+ - k_w)z]$ in eqs.(13)(or(14)) is dominantly excited. Furthermore, the wave number k_{+20} goes back to the natural wave number at around $\hat{z}$=36 where the growth rate of the f=40GHz sideband instability field disappeared. Since the ponderomotive phase velocity with f=20GHz, $v_{p20} \equiv \omega_{20}/(k_{+20}+k_w)$, is smaller than v_{p40} at $\hat{z} \simeq 36$, the f=20GHz field obtains the substantial power from the electron kinetic energy by the separatrix to overlap with the f=40GHz sideband instability wave. This feature can be seen in Figs.4(b) and (d) which represents the spatial evolution of the trapping fraction for each field, and the phase space plot of electron positions for the primary ponderomotive field. The amplitude of the forced oscillation at which the wave number k_{+20} changes $(\hat{z} \simeq 24)$ is estimated from eq.(13) as

$$\tilde{a}_{20}^{f} = \frac{2\hat{\xi}^2 \hat{\Omega}_w a_{60} a_{40}}{[k_{+20}^2 - (\Delta k_+ - k_w)^2]} \sim 3\times 10^{-8} ,$$

by employing $\xi \simeq 0.4$, $\hat{\Omega}_w \simeq 0.74$, $k_{+20} \sim \Delta k_+ \simeq 2.64 k_w$, $a_{60} \simeq 3\times10^{-2}$, and $a_{40} \simeq 2\times10^{-5}$. The estimated value of $\tilde{a}_{20}^{f}$ is one order smaller one compared with the input amplitude, i.e. $a_{20} \simeq 3\times10^{-7}$. The discrepancy is considered to originate from the other nonlinear coupling terms except $[p\times(\nabla\times A)]_z$ in motion and continuity equations.

Such a mode coupling is also observed in the linear stage where two radiation fields exponentially grow with enough powers in it. Figure 5 shows the result when f=60 and 70GHz waves which independently grow in the linear stage($\Gamma_{60} \simeq \Gamma_{70} \sim \Gamma_p$) are injected with $P_{in,60}=10^2 W/cm^2$ and $P_{in,70}=1 W/cm^2$, respectively. Besides that, f=10GHz lower frequency field, and f=50 and 80GHz symmetric sidebands with respect to primary fields are taken into account with $P_{in}=10^{-5} W/cm^2$. The space charge fields and wave numbers of the radiation are also illustrated in Fig.5(b) and (c). The coupling between the primary fields forces to excite the beam modulation ($\delta n_{10}, \delta p_{10}$) and the f=10GHz lower frequency wave with the growth rate given by $\Gamma_{10} \simeq \Gamma_{60}+\Gamma_{70} \sim 2\Gamma_p$. The radiation wave number also changes to the down shifted value from the natural one at $\hat{z} \simeq 11$ as Fig.4 case. The amplitude of the forced oscillation at $\hat{z} \simeq 11$ is estimated from eq.(13) as $\tilde{a}_{10}^{f} \sim 3\times10^{9}$, which is also one order smaller value compared with the initial input.

Figure 5 also shows that the second coupling between the primary waves(f=60 and 70GHz) and the lower frequency beam modulation ($\delta n_{10}, \delta p_{10}$) forces to excite the f=50 and 80GHz sidebands at around $\hat{z}$=14 with the growth rate given by $\Gamma_{50,70} \simeq \Gamma_{10}+\Gamma_p \simeq \sim 3\Gamma_p$ from the linear ones. The growing of sidebands is terminated owing to the saturation of the f=70GHz field. In Fig.5(c), the wave numbers of the symmetrical sidebands, k_{+50} and k_{+70}, are found to maintain the natural wave numbers in accordance with the discussion in Sec.3-2. We here note that sidebands of f=50 and 80GHz are excited even if

the f=10GHz radiation field is absent, which means that these sidebands are induced as result of not the radiation field but the beam modulation $(\delta n_{10}, \delta p_{10})$.

When the continuous noise spectrum radiations are present, such a multi-mode coupling process gives rise to the interesting result. Figure 6(a) shows the spatial evolution of the f=60GHz primary wave with an initial input power of $P_{in,60}$=10W/cm^2 when 14 different wavelength radiation fields from f=10GHz to f=80GHz (i.e. $\Delta\omega/2\pi$=5GHz and $N=\omega_r/\Delta\omega$=12) with P_{in}=10^{-3}W/cm^2 exist. It the linear stage($8\lesssim\hat{z}\lesssim18$), the f=50~80GHz parasitic waves exhibit the linear FEL amplification(see Fig.3). On the other hand, the f=10~45GHz lower frequency waves rapidly grow by the multi-mode coupling. After the saturation of the primary wave, the f=40GHz wave which has the maximum growth rate for the sideband instability first overtakes the primary one at $\hat{z}\simeq30$. The radiation power spectrum at $\hat{z}$=35 is also illustrated in Fig.6(a) together with the electron energy distribution. Here, we can see the radiation spectrum which corresponds to the linear FEL amplification and the sideband instability at around f=60GHz and f=40GHz, respectively. Furthermore, at around f=20GHz, we observe a group of the radiations induced by the mode-coupling between the saturated primary wave and the sideband instability waves around f=40GHz. The center frequency of the spectrum($f\simeq$20GHz) coincides with $f\simeq\Delta\omega_{s,max}/2\pi$ and the half width is nearly equal to that of the sideband instability. The electron energy distribution also spread a great deal to the lower γ region. Note that the total power of the radiation spectrum induced by the mode coupling($10\text{GHz}\lesssim f\lesssim30\text{GHz}$) is the same level as that by the linear FEL amplification and the sideband instability. The phase space plot for the primary wave is also shown in Fig.7 from $\hat{z}$=15 to 50. Particles diffuse to lower energy region corresponding to the particle energy distribution in Fig.6(a).

In Fig.6(a), the wiggler length $\hat{L}_s \equiv L_s/\lambda_w \simeq 11$ is an important parameter for a realistic FEL design, because $\hat{L}_s$ represents a typical length in which the quality of the radiation field and the electron energy distribution significantly changes. The trapped particle fraction $\langle\delta\rangle_{60}$ also decreases to 30% for $\hat{z} > \hat{z}_{sat} + \hat{L}_s$, although $\langle\delta\rangle_{60} \simeq 75\%$ for $\hat{z} < \hat{z}_{sat} + \hat{L}_s$ as shown in Fig.6(b). The characteristic length $\hat{L}_s$ closely relates to the ratio of the initial power between the parasitic noise field and the primary one, i.e. $\alpha \equiv P_{in,noise}/P_{in,primary}$. With an increase of α(i.e. $\alpha \to 1$), L_s becomes close to zero $L_s \to 0$ and the signal with a rather broad frequency spectrum is obtained. On the other hand, to obtain a monochromatic signal($P_{40}/P_{60} \lesssim 10^{-1}$) for a fixed wiggler length of, for instance, $\hat{L} \simeq 24$, $\alpha \lesssim 10^{-3}$ is required. In the case of the tapered wiggler FEL, the starting point of the tapering, $\hat{z}_{tap}$, should also be carefully chosen so as to satisfy the condition $0 \lesssim (\hat{z}_{tap} - \hat{z}_{sat}) \lesssim \hat{L}_s$, since the trapped particle fraction $\langle\delta\rangle_{60}$ rapidly decreases for $\hat{z} \gtrsim \hat{z}_{sat} + \hat{L}_s$.

4. Concluding Remarks

We investigated excitation mechanisms of the parasitic wave and the modulation of output signals in a high current Raman operation regime by using the one-dimensional multi-frequency amplification code. We first studied the single sideband case and found that the frequency shift $\Delta\omega_{s,max}$ and the growth rate of the sideband instability wave Γ_{sb} becomes comparable to that of the primary signal. On the basis of the single sideband analysis, we developed the analysis to cases where multi-sideband waves exist.

We found that the nonlinear coupling between two radiation fields (ω_1, ω_2) induces a beat field with $\Delta\omega = \omega_1 - \omega_2$ and corresponding momentum and density modulations. The lower frequency beam modulation forces to excite the radiation field through the coupling with the wiggler field.

In Fig.6(a), the wiggler length $\hat{L}_s \equiv L_s/\lambda_w \simeq 11$ is an important parameter for a realistic FEL design, because $\hat{L}_s$ represents a typical length in which the quality of the radiation field and the electron energy distribution significantly changes. The trapped particle fraction $\langle\delta\rangle_{60}$ also decreases to 30% for $\hat{z} > \hat{z}_{sat} + \hat{L}_s$, although $\langle\delta\rangle_{60} \simeq 75\%$ for $\hat{z} < \hat{z}_{sat} + \hat{L}_s$ as shown in Fig.6(b). The characteristic length $\hat{L}_s$ closely relates to the ratio of the initial power between the parasitic noise field and the primary one, i.e. $\alpha \equiv P_{in,noise}/P_{in,primary}$. With an increase of α(i.e. $\alpha \to 1$), L_s becomes close to zero $L_s \to 0$ and the signal with a rather broad frequency spectrum is obtained. On the other hand, to obtain a monochromatic signal($P_{40}/P_{60} \lesssim 10^{-1}$) for a fixed wiggler length of, for instance, $\hat{L} \simeq 24$, $\alpha \lesssim 10^{-3}$ is required. In the case of the tapered wiggler FEL, the starting point of the tapering, $\hat{z}_{tap}$, should also be carefully chosen so as to satisfy the condition $0 \lesssim (\hat{z}_{tap} - \hat{z}_{sat}) \lesssim \hat{L}_s$, since the trapped particle fraction $\langle\delta\rangle_{60}$ rapidly decreases for $\hat{z} \gtrsim \hat{z}_{sat} + \hat{L}_s$.

4. Concluding Remarks

We investigated excitation mechanisms of the parasitic wave and the modulation of output signals in a high current Raman operation regime by using the one-dimensional multi-frequency amplification code. We first studied the single sideband case and found that the frequency shift $\Delta\omega_{s,max}$ and the growth rate of the sideband instability wave Γ_{sb} becomes comparable to that of the primary signal. On the basis of the single sideband analysis, we developed the analysis to cases where multi-sideband waves exist.

We found that the nonlinear coupling between two radiation fields (ω_1, ω_2) induces a beat field with $\Delta\omega = \omega_1 - \omega_2$ and corresponding momentum and density modulations. The lower frequency beam modulation forces to excite the radiation field through the coupling with the wiggler field.

Furthermore, the lower frequency modulation secondly couples to primary waves and excite the new beam modulation with $(\omega_1+\Delta\omega, \Delta\omega_2-\Delta\omega)$. The new frequency modulation also forces to excite the new radiations. The above process is systematically repeated and causes the symmetric field excitation with respect to the primary signals. Such a symmetric creation of sidebands are also studied by E.J.Sternbach in the wave guide FEL[13]. The growth rate of the radiation induced by the mode coupling is expressed by the sum of the growth rate of signal fields following additive law. Therefore, when the signal waves are growing, the growth rate of the mode coupling wave becomes larger with an increasing number of couplings. On the other hand, when the signal waves are both stable, the mode coupling waves are stable.

In the multi-frequency calculation as Fig.6, which covers the entire single sideband spectrum, the radiation spectrum is unstable especially in the low frequency region until the sideband instability wave with a maximum growth rate(i.e. $\omega\simeq\omega_0-\Delta\omega_{s,max}$) saturates. This is due to the fact that the ponderomotive phase velocity $v_p=\omega/(k_++k_w)$ for low frequency waves is smaller than that of the primary one, i.e. $v_p<v_{pm=0}=\omega_{m=0}/(k_{+m=0}+k_w)$, and the separatrix overlapping among these waves creates the channel to diffuse electrons to a lower energy region. The electron diffusion, in turn, amplifies the radiation field. On the other hand, the phase velocities of the high frequency ponderomotive field which is induced by the mode coupling are larger than that of the primary one, i.e. $v_p>v_{pm=0}$. Therefore, even if the separatrix overlapping with the primary wave takes place, the electron diffusion to a higher energy region reduces the radiation field energy, which means stable. Here, we note that the multi-mode coupling described here significantly modulates the output radiation spectrum when $\Delta\omega_{s,max}\sim\Delta\omega_{FEL}\sim(1/4\text{-}1/2)\omega_0)$ is roughly satisfied. When $\Delta\omega_{s,max}$(or $\Delta\omega_{FEL}$)$\ll\omega_0$, the lower frequency wave($\omega\sim\Delta\omega_{s,max}$) induced by the mode coupling will saturate

in a lower level since the phase velocity of that wave, i.e. $\Delta\omega_{s,max}/(k_{+s,max}+k_w)$, is too low to cause the separatrix to overlap with the sideband instability wave.

In the paper, we employed the free boundary 1-dimensional model which does not include wave guide effects[13,14]. The excitation of lower frequency parasitic waves may be suppressed by adjusting the wave guide dimension so as to satisfy the condition $\Delta\omega_{s,max} \lesssim \omega_c$, where ω_c is the cut-off frequency of the wave guide.

Acknowledgment

We express sincere thanks to prof. K.Mima, prof. A.Gover, and Dr. S.Tokuda for their useful discussions and comments. Thanks are also due to Dr. H.Maeda, Dr. T.Takeda, and Dr. M.Tanaka for their continuous encouragement.

in a lower level since the phase velocity of that wave, i.e. $\Delta\omega_{s,max}/(k_{+s,max}+k_w)$, is too low to cause the separatrix to overlap with the sideband instability wave.

In the paper, we employed the free boundary 1-dimensional model which does not include wave guide effects[13,14]. The excitation of lower frequency parasitic waves may be suppressed by adjusting the wave guide dimension so as to satisfy the condition $\Delta\omega_{s,max} \lesssim \omega_c$, where ω_c is the cut-off frequency of the wave guide.

Acknowledgment

We express sincere thanks to prof. K.Mima, prof. A.Gover, and Dr. S.Tokuda for their useful discussions and comments. Thanks are also due to Dr. H.Maeda, Dr. T.Takeda, and Dr. M.Tanaka for their continuous encouragement.

References

1) N.M.Kroll, P.L.Moton, and M.N.Rosenbluth, IEEE J.Quantum Electron. QE-17, 1436(1981).

2) R.C.Davidson and J.S.Wurtele, Phys.Fluids 30, 557(1987).

3) R.C.Davidson and J.S.Wurtele, Phys.Fluids 30, 2825(1987).

4) S.R.Riyopoulos and C.M.Tang, Phys.Fluids 31, 1708(1988).

5) D.C.Quimby, J.M.Slater, and J.P.Wilcoxon, IEEE J. Quantum Electron QE-21, 979(1986).

6) B.Hafizi, A.Ting, P.Sprangle, and C.M.Tang, Phys.Rev.A38, 197(1988).

7) W.B.Colson, Nuc. Instr. and Meth., BT(A250), 168(1987).

8) A.T.Lin, Phys.Rev.Lett. 46,1515(1981).

9) Y.Kishimoto, H.Oda, M.Shiho, Phys. Rev. Lett.,65,851(1990).

10) Y.Kishimoto, H.Oda, M.Shiho, K.Odajima, and H.Maeda, J.Phy.Soc.Jpn.59, 118(1990).

11) A ratio between f_{es} and the ponderomotive force f_p is estimated for a primary wave as $|f_{es}/f_p| = 2\xi^2\gamma^2 k_w^2 c\langle\delta\rangle |H(\psi,\psi_e)| / a_w a_{m=0}\omega(k_+ + k_w)$, where $\xi \equiv \omega_b/\gamma_b^{1/2} c k_w$, and $H(\psi,\psi_e)$ denotes the phase factor given by $H = \langle\beta_{z0}\cos\psi_e\rangle$ $(\sin\psi_e/\sin\psi)$[7]. From the above relation, we estimates the ratio as $|f_{es}/f_p| = 0.5\sim1.5$ in $20\lesssim\hat{z}\lesssim30$.

12) $\Gamma_{20,a}$ tends to $\Gamma_{20,b}$ in $\hat{z}_{sat}\lesssim\hat{z}\lesssim35$ by introducing the axial beam energy spread $\Delta\gamma_b$ which reduces f_{es} through a reduction of $H(\psi,\psi_e)$ in Ref.8.

13) E.J.Sternbach, IEEE Transaction on Plasma Science, 18, 460(1990).

14) W.M.Sharp and S.S.Yu, Nucl.Instr. and Meth., A272, 397(1988).

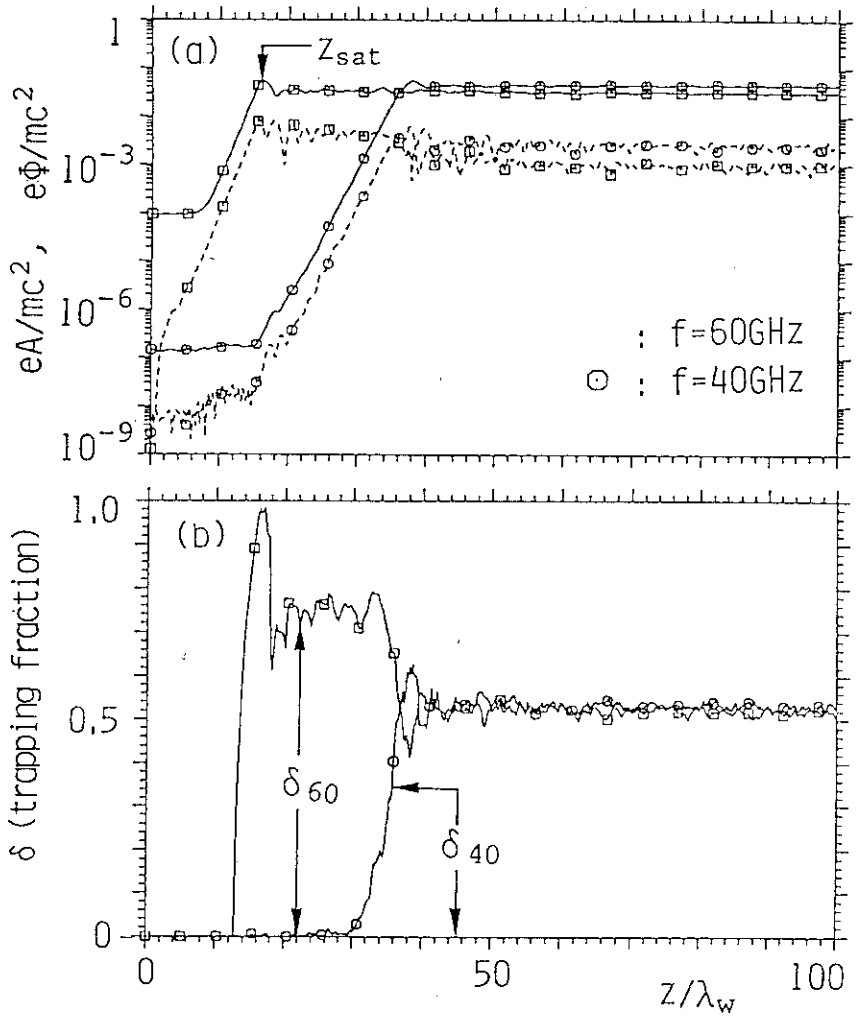

Fig. 1 (a) Spatial evolution of the radiation field(solid line) and the space charge field(dashed line) for f=40GHz ($P_{in,40}=10^{-3}W/cm^{-2}$) and f=60GHz ($P_{in,60}=10^{-3}W/cm^{-2}$) waves.

(b) Spatial evolution of the trapping fraction δ due to ponderomotive potential.

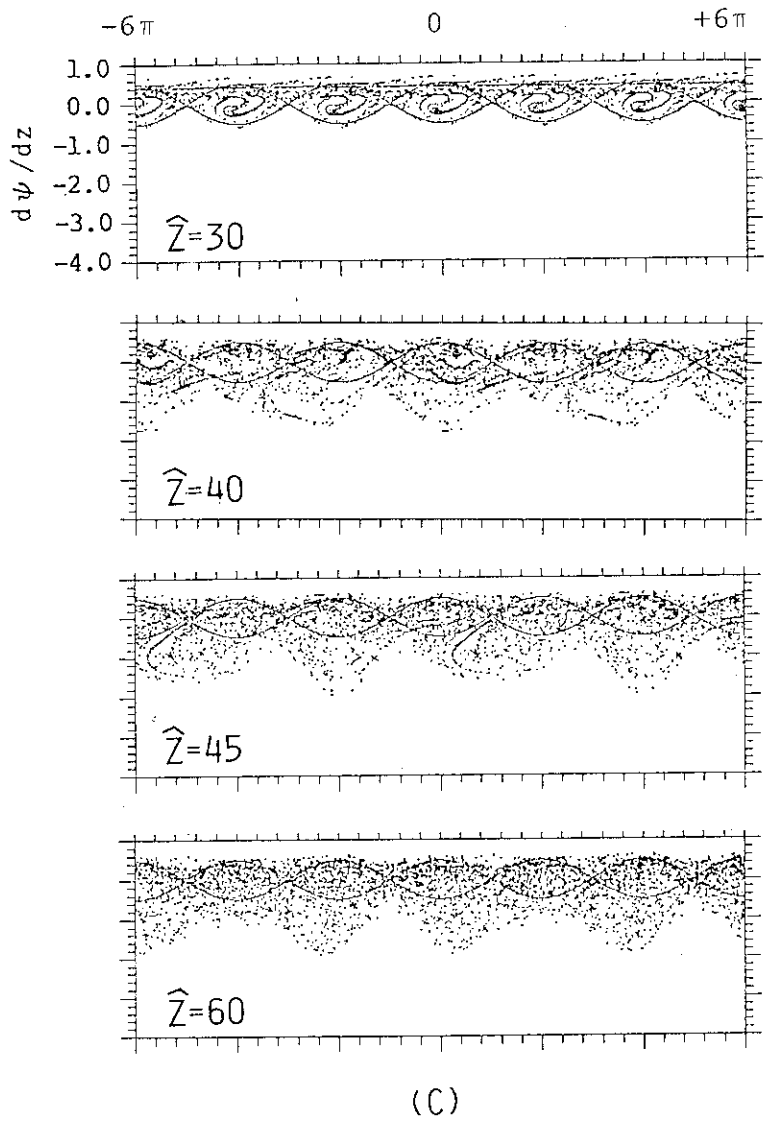

Fig. 1 (c) Phase space plot of particles for the primary ponderomotive potential, ($\psi_{m=0}$, $d\psi_{m=0}/dz$). Solid line represents the separatrix.

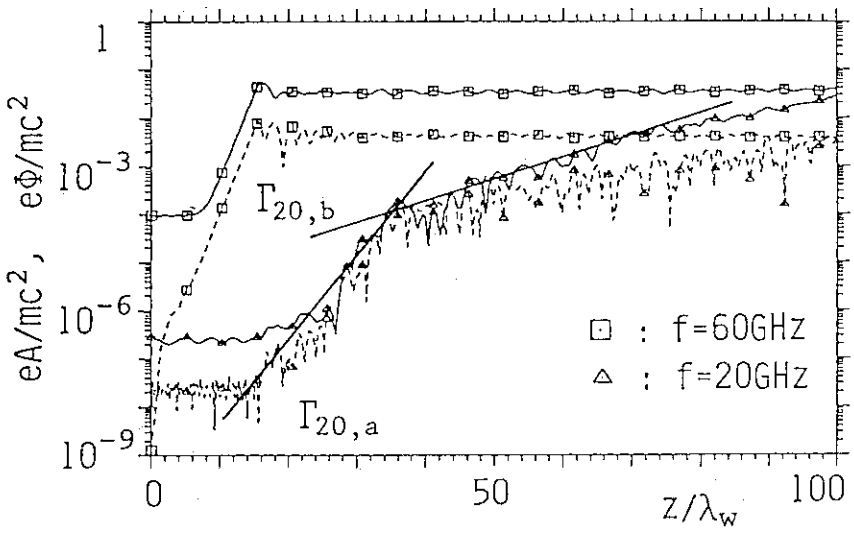

Fig. 2 Spatial evolution of the radiation field(solid line) and the space charge field(dashed line) for f=20GHz ($P_{in,\,20}=10^{-3}W/cm^{-2}$) and f=60GHz ($P_{in,\,60}=10^{-3}W/cm^{-2}$) waves.

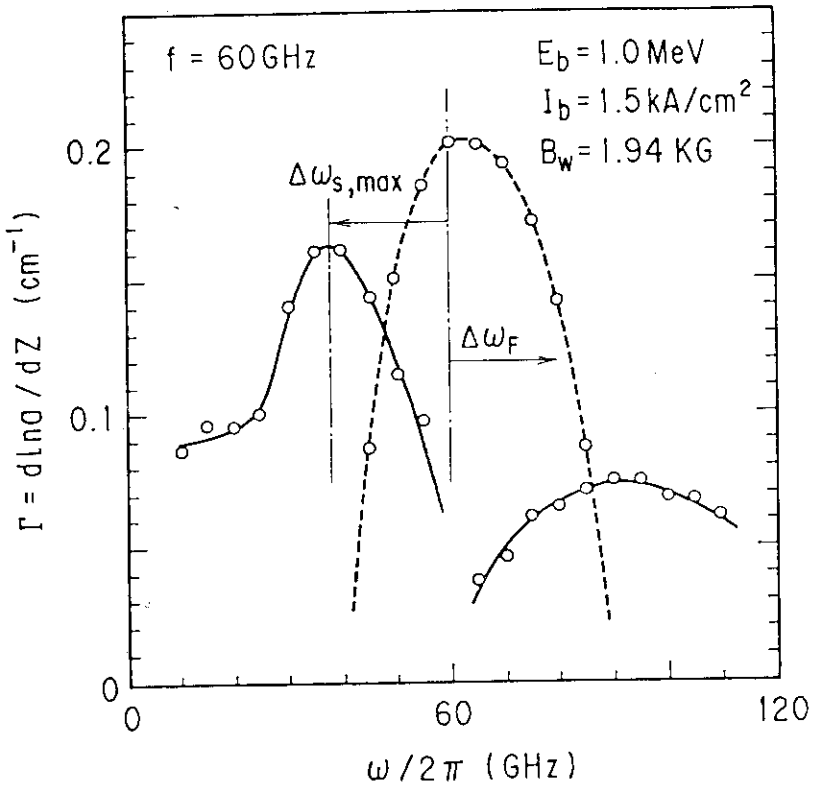

Fig. 3 Frequency spectrum of single sideband instability in the presence of the f=60GHz primary wave. Dashed line represents the linear FEL growth rate.

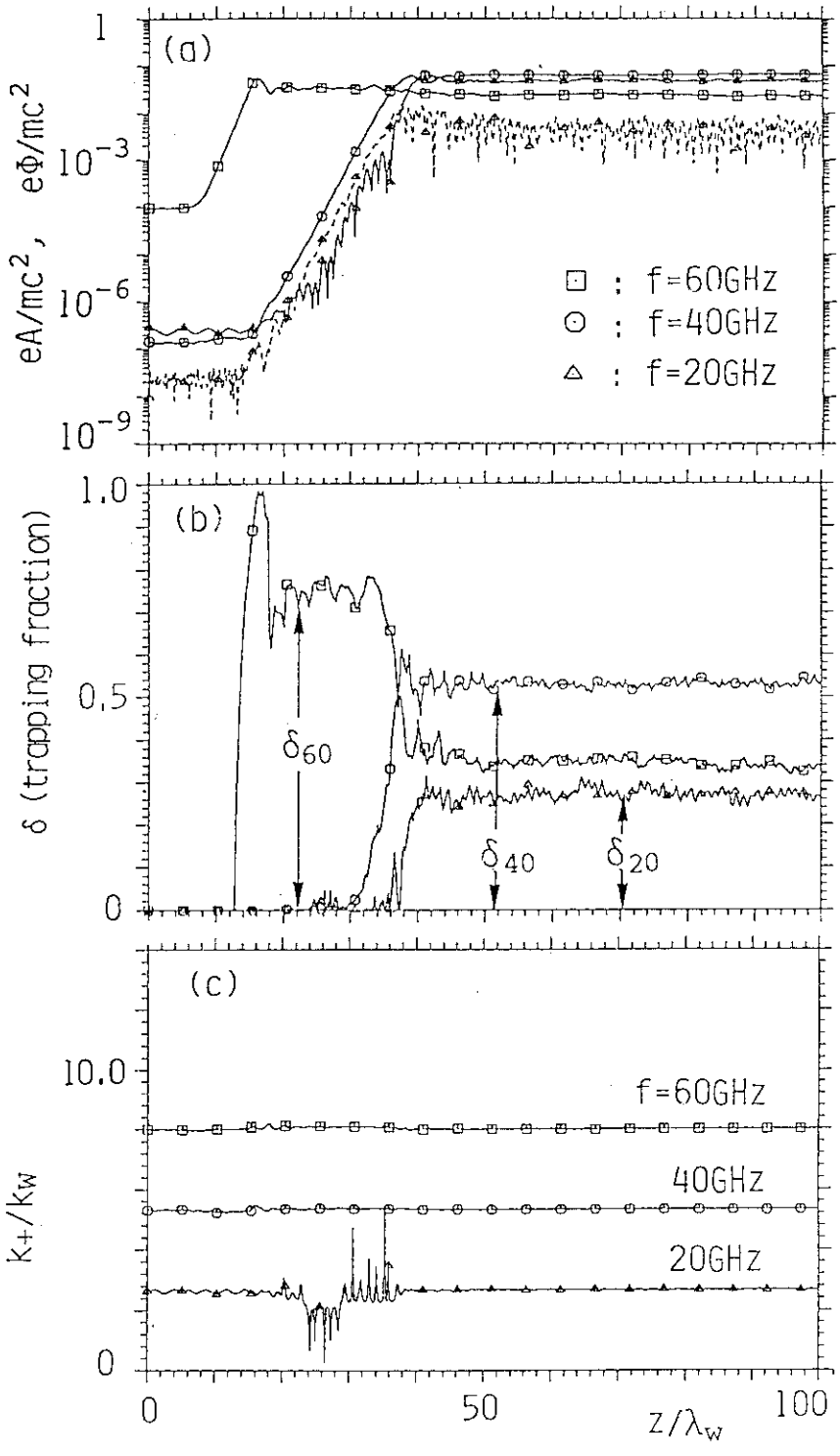

Fig. 4 Spatial evolution of the radiation field(a), trapping fraction(b), and the wave number of radiation fields(c) for f=60GHz wave and f=20 and 40GHz sidebands. Dashed line in (a) represents the space charge field of the f=20GHz wave.

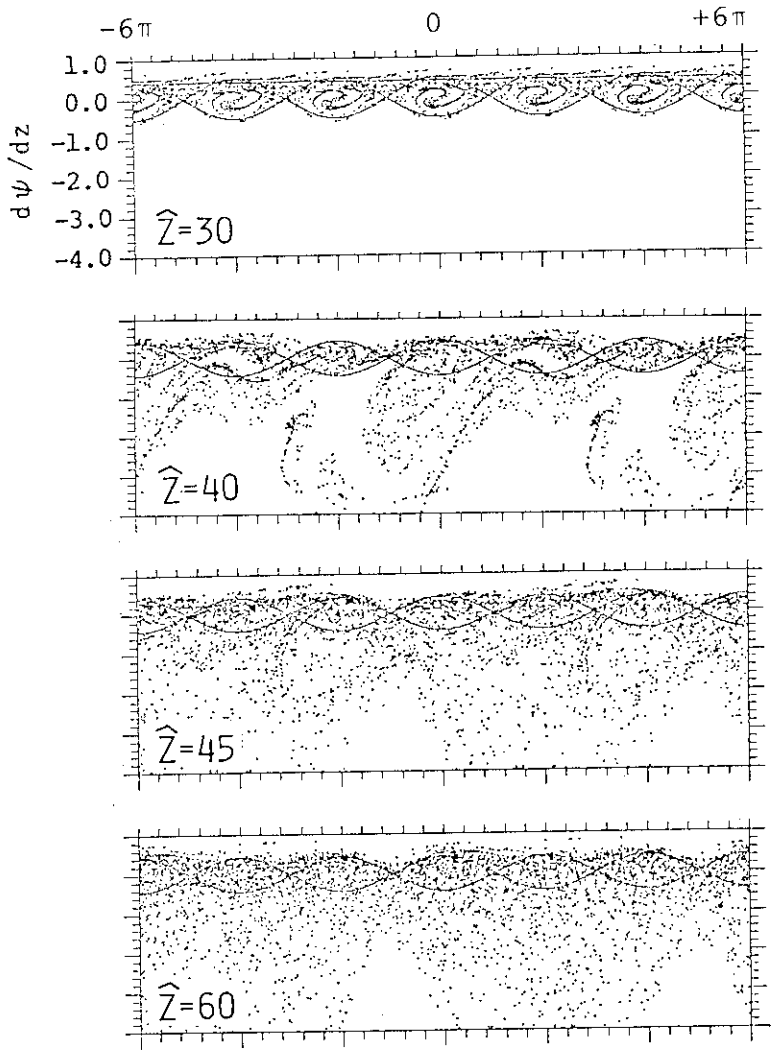

(d)

Fig. 4 (d) Phase space plot of particles for the primary ponderomotive potential, ($\psi_{m=0}$, $d\psi_{m=0}/dz$). Solid line represents the separatrix.

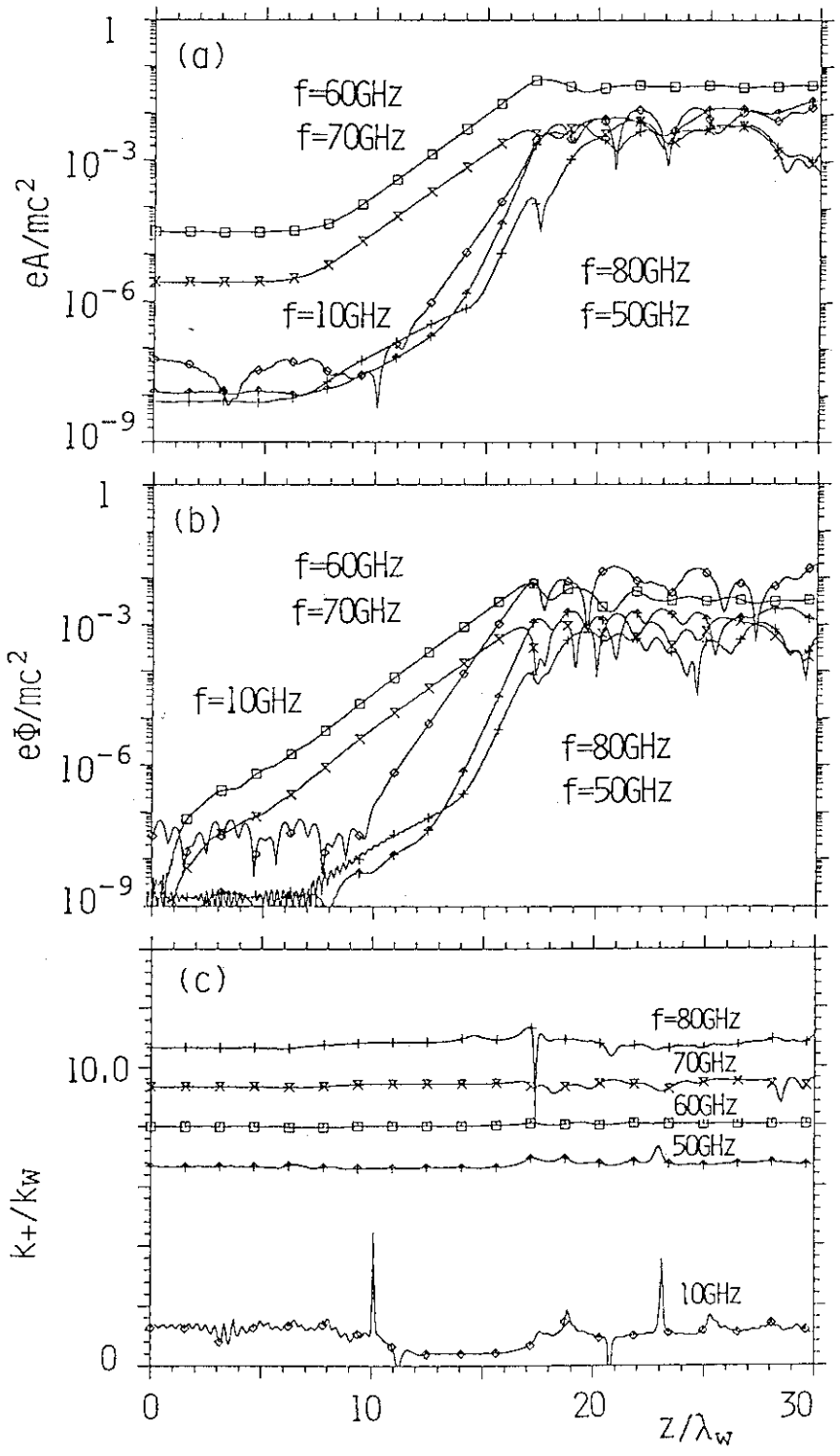

Fig. 5 Spatial evolution of radiation field(a) trapping fraction(b), and the wave number of radiation field(c) for f=60GHz ($P_{in,60}=10^{2}W/cm^{2}$) and f=70GHz ($P_{in,70}=10^{2}W/cm^{2}$) primary waves, and f=10, 50, 80GHz sidebands ($P_{in}=10^{-5}W/cm^{2}$).

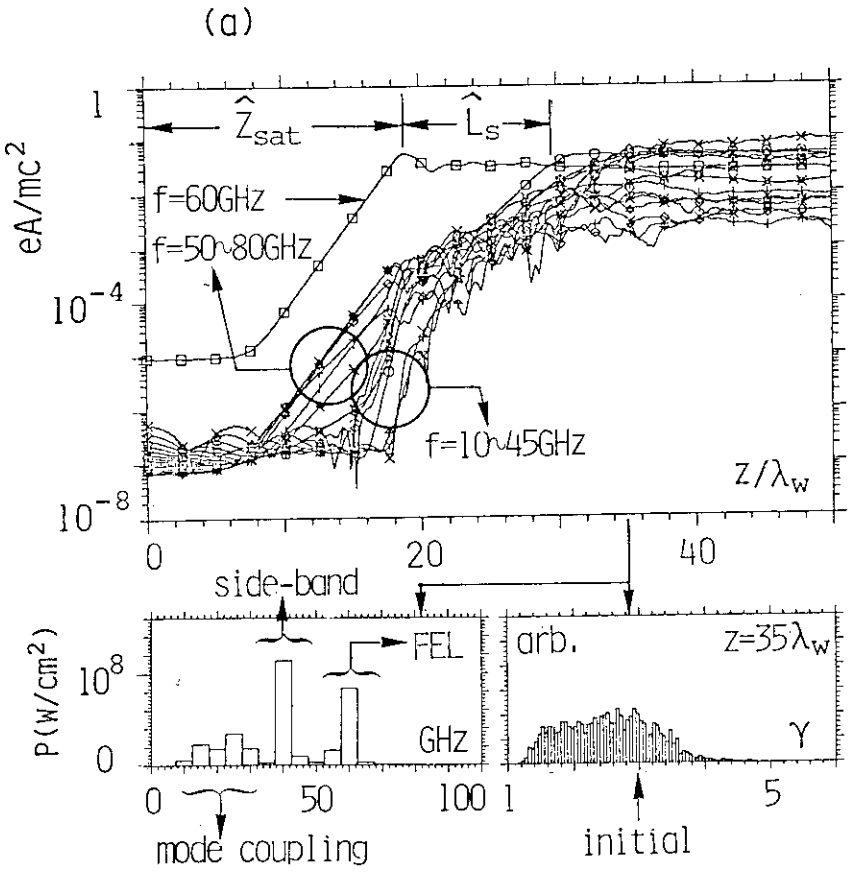

Fig. 6 (a) Spatial evolution of the radiation field for f=60GHz ($P_{in,60}$=10W/cm^2) wave and 14 sidebands from f=10GHz to 80GHz(P_{in}=10^{-3}W/cm^2). Frequency spectrum and electron γ distribution at $\hat{z}$=35 are also shown.

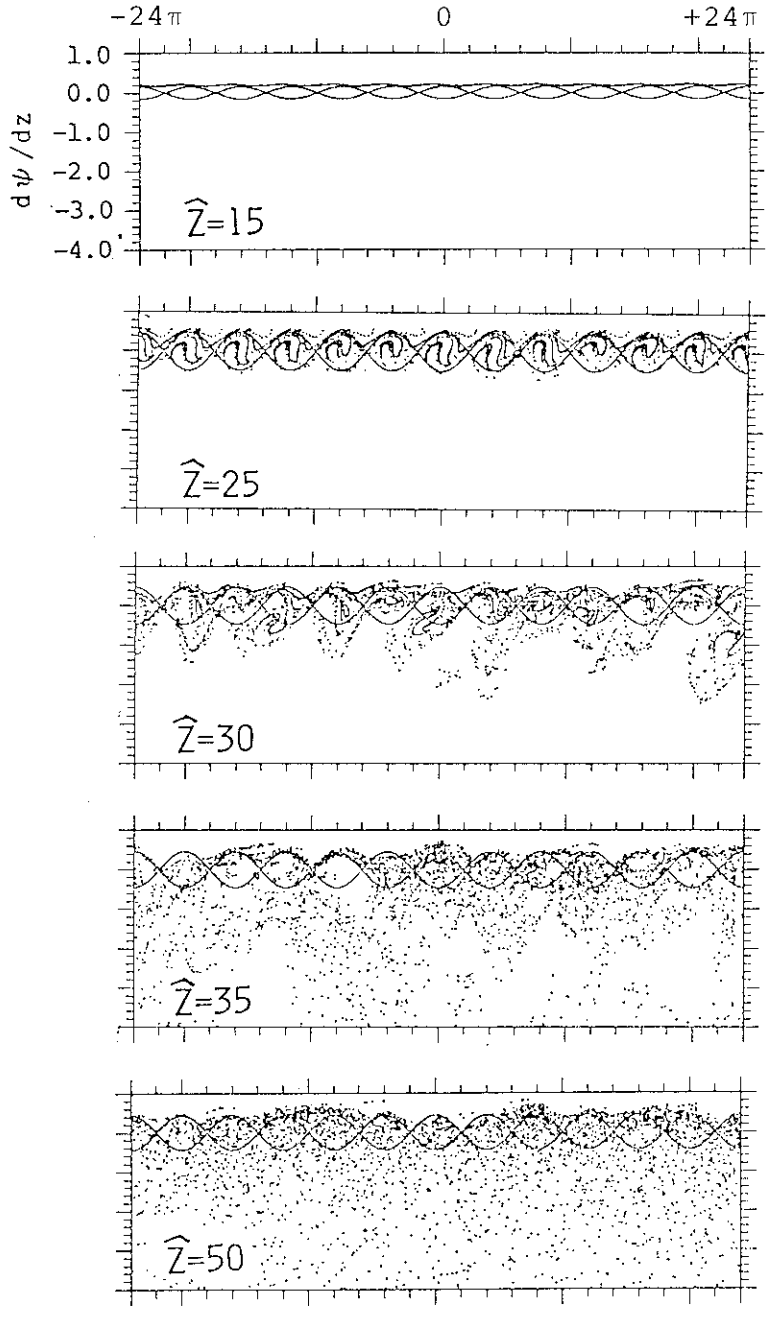

Fig. 6 (b) Phase space plot of particles for the primary ponderomotive potential, ($\psi_{m=0}$, $d\psi_{m=0}/dz$). Solid line represents the separatrix.